

Manuscript Number: GCA-D-15-00578

Title: Hydrous melting and H₂O partitioning in and above the mantle transition zone: insights from water-rich MgO-SiO₂-H₂O experiments}

Article Type: Article

Corresponding Author: Dr. Robert Myhill, Ph.D.

Corresponding Author's Institution: Bayerisches Geoinstitut

First Author: Robert Myhill, Ph.D.

Order of Authors: Robert Myhill, Ph.D.; Daniel J Frost, Ph.D.; Davide Novella, Ph.D.

Abstract: Hydrous melting at high pressures affects the physical properties, dynamics and chemical differentiation of the Earth. However, probing the compositions of hydrous melts at the conditions of the mantle transition zone has traditionally been challenging. In this study, we conducted high pressure multianvil experiments at 13 GPa between 1200 and 1900 °C to investigate the liquidus in the system MgO-SiO₂-H₂O. Water-rich starting compositions were created using platinic acid (H₂Pt(OH)₆) as a novel water source. As MgO:SiO₂ ratios decrease, the T-X_{H₂O} liquidus curve develops an increasingly pronounced concave-down topology. The melting point reduction of enstatite and stishovite at low water contents exceeds that predicted by simple ideal models of hydrogen speciation. We discuss the implications of this work on the behaviour of melts in the deep upper mantle and transition zone, and present new models describing the partitioning of water between the olivine polymorphs and associated hydrous melts.

Suggested Reviewers: Natalie Bolfan-Casanova Ph.D.
Chargé de Recherche, Laboratoire Magmas et Volcans, IPG-Clermont Ferrant
n.bolfan@opgc.univ-bpclermont.fr

Marc Hirschmann Ph.D.
Professor, Earth Sciences, University of Minnesota
mmh@umn.edu

Joe Smyth Ph.D.
Geological Sciences, University of Colorado at Boulder
Smyth@colorado.edu

Craig Manning Ph.D.
Professor, Earth and Space Sciences, UCLA
manning@ess.ucla.edu

Lena Melekhova Ph.D.
Earth Sciences, University of Bristol
lena.melekhova@bristol.ac.uk

August 2, 2015

Dear editor,

Please find attached a manuscript describing our recent work on high pressure hydrous melts, which we hope you will consider for publication as an *Article* in *Geochimica et Cosmochimica Acta*. Our study is entitled *Hydrous melting and partitioning in and above the mantle transition zone: insights from water-rich MgO-SiO₂-H₂O experiments*, with three authors:

- Dr Robert Myhill, corresponding author)
- Prof. Daniel Frost, also from the Bayerisches Geoinstitut
- Dr Davide Novella, Laboratoire Magmas et Volcans, Université Blaise Pascal

Our manuscript describes the first ultrahigh pressure experiments on MgO-SiO₂-H₂O compositions more water-rich than the brucite-quartz binary. We accomplish this by using a new water source, dihydrogen hexahydroxyplatinate, which breaks down to PtO₂ and H₂O at high temperatures. Our compositions help us to explore regions of the ternary system which have been traditionally difficult to reach. These regions include the melt compositions expected within the Earth's interior, and so help us to constrain melt productivity within subducting slabs and around the mantle transition zone.

In addition to constraining the liquidus in water-rich systems, we build a simple melt model for the forsterite-water binary that allows us to model H₂O activities. Using this data, we construct thermodynamic models for water incorporation into the olivine polymorphs at high pressure.

We confirm that the accompanying manuscript is original work, not published elsewhere or under consideration for publication elsewhere. We have no financial conflicts.

Best wishes,

Robert Myhill
Bayerisches Geoinstitut
Universität Bayreuth
95440 Bayreuth
Deutschland
Tel: +49-(0) 921 55 3746
[mailto: myhill.bob@gmail.com](mailto:myhill.bob@gmail.com)

Hydrous melting and partitioning in and above the mantle transition zone: insights from water-rich MgO-SiO₂-H₂O experiments

R. Myhill, D. J. Frost

Bayerisches Geoinstitut, Universität Bayreuth, Universitätsstrasse 30, 95447 Bayreuth, Germany

D. Novella

Laboratoire Magmas et Volcans, Université Blaise Pascal, 5 Rue Kessler, 63038 Clermont-Ferrand, France

Abstract

Hydrous melting at high pressures affects the physical properties, dynamics and chemical differentiation of the Earth. However, probing the compositions of hydrous melts at the conditions of the mantle transition zone has traditionally been challenging. In this study, we conducted high pressure multianvil experiments at 13 GPa between 1200 and 1900 °C to investigate the liquidus in the system MgO-SiO₂-H₂O. Water-rich starting compositions were created using platonic acid (H₂Pt(OH)₆) as a novel water source. As MgO:SiO₂ ratios decrease, the T- X_{H_2O} liquidus curve develops an increasingly pronounced concave-down topology. The melting point reduction of enstatite and stishovite at low water contents exceeds that predicted by simple ideal models of hydrogen speciation. We discuss the implications of this work on the behaviour of melts in the deep upper mantle and transition zone, and present new models describing the partitioning of water between the olivine polymorphs and associated hydrous melts.

Keywords: high pressure, mantle, hydrous melting, water, liquidus

*Corresponding author: R. Myhill

Email address: myhill.bob@gmail.com (R. Myhill, D. J. Frost)

1. Introduction

Hydrous melts have a remarkable influence on Earth’s surface and interior. Melting at subduction zones is primarily driven by the release of hydrous fluids from the warming slab at about 100 km depth, producing the world’s arc volcanoes. The water cycle does not stop here, however; hydrous minerals within the crust should allow some water to be transported to 250 km (Poli and Schmidt, 2002), and peridotite hydration should allow water to penetrate into the mantle transition zone or deeper, providing it remains low enough in temperature (Komabayashi et al., 2005). This deep water cycle must extend to at least 500 km depth, as implied by the discovery of water-saturated ringwoodite in a diamond from Juina, Brazil (Pearson et al., 2014). In addition to kimberlites and arc volcanoes, hydrous melts are known to metasomatise and refertilise the lithospheric mantle, creating the so-called MARID (mica, amphibole, rutile, ilmenite, diopside) assemblage. It has also been argued that neutral or negatively buoyant water-rich melts are to blame for low velocity and high conductivity layers observed at the 410 km discontinuity, and that these small fraction melts could act to filter out incompatible elements during upwelling (Bercovici and Karato, 2003).

Processes involving deep-seated hydrous melts are controlled to a great extent by melt composition. Most importantly, the equilibrium proportion of H_2O in melts controls the extent of partial melting for a given bulk H_2O content. Together with solid-solid-melt dihedral angles, the extent of partial melting governs the permeability and therefore mobility of melt, and the ability to detect it via body wave seismology and electrical conductivity measurements. Composition is also a key variable in determining melt density and viscosity. Finally, the change in equilibrium melt compositions with pressure and temperature has a significant influence on melt channelisation, which reduces melt-solid interaction and increases ascent rates.

Melt compositions are also required to understand the stability of dense hydrous magnesium silicate (DHMS) phases and the water capacity of nominally

anhydrous minerals (NAMS) at high pressure. Together, these control water transport and storage in the deep mantle, and as such are the primary inputs to models of the water budget of the Earth. Hydrous fluids at elevated pressures and temperatures cannot be treated as pure H₂O. As pressure increases, immiscibility between fluid and melt decreases, and the thermal stability of hydrous phases increases. As a result, fluids/melts released by the breakdown of hydrous phases have H₂O activities significantly lower than one. Understanding and predicting the P - T conditions of DHMS phase breakdown and the water storage capacity at of NAMS therefore requires good activity-composition models for hydrous melts.

Constraining melt compositions remains a major challenge in high-pressure experimental petrology. The primary problem is that water-rich melts are unquenchable. During quench, some of the water in the melt crystallises as hydrous minerals such as brucite, but a significant proportion crystallises as water ice at high pressure, which is then lost as water vapour on decompression and sample preparation. The original H₂O contents of the partial hydrous melts are normally estimated by mass balance and/or by deficits in microprobe totals (e.g. Ohtani et al., 2000; Demouchy et al., 2005; Litasov et al., 2011; Melekhova et al., 2007). Mass balance alone depends on knowing the volume proportions of solid phases and quench phases, being able to recognise and subtract quench overgrowths where they exist, and knowing the effective ambient-pressure density of the melt. All of these are associated with significant uncertainties. Deficits in microprobe totals are sometimes reasonable for estimating water contents in solid phases, provided the microprobe standards are suitable, and the microprobe is exceptionally well-calibrated (even a small deficit would imply a large water content). However, for quench melts the deficits are attributable to water held in quench phases *and* porosity within the volume sampled by the defocused beam. For this reason, defocused beam techniques should probably be restricted to estimating non-volatile element ratios (such as Mg:Si).

Bracketing the liquidus requires only that the bulk composition during the experiment is known. This technique therefore seems a good alternative to esti-

mating melt compositions ex-situ. The only problem is that at slab or ambient
 mantle temperatures, water contents in melts at high pressure are very high.
 Making up solid starting compositions with more water than a brucite-quartz
 65 mix has traditionally been avoided. Existing studies either extrapolate high
 temperature liquidus curves to high water contents or add water in liquid form
 if the sample chambers are sufficiently large (e.g. Hunt and Manning, 2012). Ex-
 trapolation is prone to large errors, and accurately adding liquid water to the
 small volumes of high pressure capsules is essentially impossible. In this study,
 70 we use high purity platinic acid, hexahydroxyplatinate(IV) ($\text{H}_2\text{Pt}(\text{OH})_6$), as a
 novel water source. Platinic acid is a pale yellow compound which is stable to
 about 130 °C (Nagano, 2002). It breaks down at higher temperatures, releasing
 four molecules of H_2O and forming platinum (IV) oxide PtO_2 . Its relatively
 high stability, high water content and the inert nature of the breakdown prod-
 75 uct (in a system where redox reactions are absent) make it an excellent water
 source for high pressure hydrous melting experiments.

2. Experimental and analytical methods

Starting compositions were created from a mixture of high-purity brucite,
 quartz and platinic acid ($\text{H}_2\text{Pt}(\text{OH})_6$). Before weighing, quartz was dried at
 80 1000 °C for 12 hours, while brucite was heated to 250 °C, also over 12 hours.
 Both powders were stored in a desiccating oven at 130 °C. Platinic acid is
 hygroscopic, so was stored in a vacuum desiccator. Powders were weighed and
 ground dry in an agate mortar for 30 minutes, using a mask, goggles and gloves
 to avoid physical contact with the platinic acid. Starting compositions were
 85 stored in glass vials in a vacuum desiccator. Compositions are listed in Table 1.

Capsules were created from 2 mm-diameter $\text{Pt}_{90}\text{Rh}_{10}$ and Au rods, cut by
 wire saw into 1 mm thick disks. Into each disk were spark-eroded two rows of
 three holes, each 250 microns in diameter and 700 microns deep. The capsules
 were cleaned by cycling between an acetone ultrasonic bath (15 minutes) and
 90 1000 °C furnace (20 minutes) three times. Any remaining contamination was

Table 1: Starting compositions

	Oxide proportions (mol%)			Compound fractions (mol/mol)		
	MgO	SiO ₂	H ₂ O	Mg(OH) ₂	SiO ₂	H ₂ Pt(OH) ₆
br 5.0	50.000	0.000	50.000	1.000	0.000	0.000
br 5.5	45.000	0.000	55.000	0.947	0.000	0.053
br 6.0	40.000	0.000	60.000	0.889	0.000	0.111
br 6.5	35.000	0.000	65.000	0.824	0.000	0.176
br 7.0	30.000	0.000	70.000	0.750	0.000	0.250
en 6.0	30.000	30.000	40.000	0.480	0.480	0.040
en 7.0	26.667	26.667	46.667	0.457	0.457	0.086
en 8.0	23.333	23.333	53.333	0.431	0.431	0.138
en 9.0	20.000	20.000	60.000	0.400	0.400	0.200
fo 11.5	36.000	18.000	46.000	0.637	0.319	0.044
fo 13.0	32.000	16.000	52.000	0.604	0.302	0.094
fo 14.5	28.000	14.000	58.000	0.566	0.283	0.152
fo 16.0	24.000	12.000	64.000	0.522	0.261	0.217
q 1.5	0.000	85.000	15.000	0.000	0.958	0.042
q 2.0	0.000	80.000	20.000	0.000	0.941	0.059
q 2.5	0.000	75.000	25.000	0.000	0.923	0.077
q 3.0	0.000	70.000	30.000	0.000	0.903	0.097
q 3.5	0.000	65.000	35.000	0.000	0.881	0.119
q 4.0	0.000	60.000	40.000	0.000	0.857	0.143
q 4.5	0.000	55.000	45.000	0.000	0.830	0.170
q 5.0	0.000	50.000	50.000	0.000	0.800	0.200
br+q 2.25	25.000	50.000	25.000	25.000	50.000	0.000
br+q 2.70	30.000	40.000	30.000	30.000	40.000	0.000
br+q 3.2	35.556	28.889	35.556	35.556	28.889	0.000
br+q 3.4	37.778	24.444	37.778	37.778	24.444	0.000

removed with a $W_{75}Re_{25}$ needle followed by a further trip to the ultrasonic bath. Capsule chambers were filled with powders of different compositions using a $W_{75}Re_{25}$ needle. Small pieces of tape were used to temporarily cover the other holes to avoid contamination.

95 Multianvil experiments were performed in the 5000 tonne press at the Bayerisches Geoinstitut (BGI). Cr-doped MgO octahedral multianvil assemblies with 18 mm edge length were used (Figure 1). Two capsules were loaded into each assembly, with the open ends of the chambers facing each other and separated by six 0.05 mm thick $Pt_{90}Rh_{10}$ or Au foils. The assemblies were compressed to 13 GPa over four hours between eight tungsten carbide cubes with
100 truncations of edge-length 11 mm. Pressure calibrations and details of the press can be found in Frost et al. (2004) and Keppler and Frost (2005). The assemblies were then resistively heated via a stepped $LaCrO_3$ heater. The temperature was recorded using a $W_{97}Re_3$ – $W_{75}Re_{25}$ (Type D) thermocouple inserted axially
105 into the assembly. To avoid water loss, higher temperature runs were heated for a shorter duration. The experiments were quenched by cutting power to the heater. The assemblies were then decompressed to room pressure over 1000 minutes.

Capsules were recovered from the assembly, separated by wire saw and then
110 ground by hand to reveal the tops of each capsule chamber. The wire saw was then used again to split the two sets of three chambers from each capsule. Each half-capsule was mounted in epoxy and mirror-polished. After revealing the edge of the capsule chambers, it was necessary to impregnate them with epoxy under vacuum before further polishing, in order to fill in the porous spaces
115 created by the hydrous melt. Grinding under running water helped remove plucked grains from the polishing surface. Prepared and cleaned samples were then coated with a 10 nm thick carbon layer.

Analysis of run products was conducted via scanning electron microscope (SEM), using BSE imaging and EDS for phase identification (via the INCA
120 software package).

3. Modelling water solubility in melts

3.1. Background

Oxygen in neutral MSH melt species can exist either as molecular water, as a bridging oxygen between magnesium and/or silicon atoms, or as part of a terminal hydroxyl group. The general equation describing the reaction between melt species is



where the subscripts br and tm respectively refer to bridging and terminal oxygens. The equilibrium between these species can be described with an equilibrium constant K (e.g. Stolper, 1982)

$$K_{(1)} = \frac{X_{\text{OH}_{tm}^-}^2}{X_{\text{H}_2\text{O}} X_{\text{O}_{br}^{2-}}} \quad (2)$$

The equilibrium constant is related to the energy $\Delta G_{(1)}$ required to protonate two bridging oxygens with a water molecule

$$K_{(1)} = \exp\left(\frac{-\Delta G_{(1)}}{RT}\right) \quad (3)$$

These equations can be used to describe in an average sense a range of melt-melt equilibria involving monomers ($\text{Mg}(\text{OH})_2$ and $\text{Si}(\text{OH})_4$), dimers ($\text{Mg}_2\text{O}(\text{OH})_2$, $\text{MgSiO}(\text{OH})_4$, $\text{Si}_2\text{O}(\text{OH})_6$) and higher oligomers. A high proportion of monomers and dimers exist in relatively dilute solutions, but not in the concentrated solutions investigated in this study.

A number of models have been presented to investigate the behaviour of concentrated hydrous melts. Silver and Stolper (1985) made the assumption that H_2O , O_{br}^{2-} and OH_{tm}^- mix ideally, with a parameter r representing the number of oxygen atoms in each formula unit which are available for protonation. For example, an Mg_2SiO_4 melt with $r = 4$ and $K_{(1)} = \infty$ represents a continuum between an anhydrous melt and one made of $\text{Mg}(\text{OH})_2$ and $\text{Si}(\text{OH})_4$ monomers. No distinction is made between isolated oligomers and partial depolymerisation of a silicate network; in other words, the energy required to form a terminal

OH group is independent of local environment. Fixing r places an implicit constraint on the maximum value of $K_{(1)}$ in water-rich compositions. For example, if $r = 1$ in a hydrated MgO melt, then water contents exceeding 50 mol% require that $K_{(1)} < \infty$. In practise, the equilibrium constant $K_{(1)}$ has been shown to be dependent on temperature and composition. Shen and Keppler (1995) obtained a good fit to isochemical data with an expression of the form

$$\Delta G_{(1)} = a + bT \quad (4)$$

Tenner et al. (2012) simplified the model of Silver and Stolper (1985) by assuming that all hydrogen in the melt exists as OH^- , and that protonation is equally likely on any oxygen ($K_{(1)} = \infty$, $\Delta G_{(1)} = -\infty$, r maximised). Deviations from this model must increase with increasing water content, and such a model cannot describe any melt more water-rich than the $\text{Mg}(\text{OH})_2\text{-Si}(\text{OH})_4$ binary.

To describe melting in the $\text{SiO}_2\text{-H}_2\text{O}$ system, Hunt and Manning (2012) generalised the aforementioned models by allowing non-ideality between the two endmembers. The excess term $\Delta G_{(1)}(\text{P}, \text{T})$ for the formation of OH^- groups was assumed to be independent of composition; all oxygens are equally available for protonation, and the local extent of protonation does not affect the energy required for each further protonation.

These models can be used to calculate melt compositions by equating the gibbs free energy of the solid G_{solid}^s with the chemical potential of the component with the composition of that solid in the melt μ_{melt}^s :

$$G_{\text{solid}}^s = \mu_{\text{melt}}^s = G_{\text{melt}}^s - RT \ln a_{\text{melt}}^s \quad (5)$$

In this study, we use the thermodynamic dataset of Stixrude and Lithgow-Bertelloni (2011) to calculate G_{solid}^s for periclase, forsterite and its high pressure polymorphs, orthoenstatite, high pressure clinoenstatite, stishovite and coesite. A modified version of the molecular dynamics-derived anhydrous melt model of de Koker et al. (2013) is used to calculate G_{melt}^s , and the Silver and Stolper (1985) model is used to calculate a_{melt}^s . The calculations in the work were

undertaken with the mineral physics toolkit Burnman (available from <https://geodynamics.org/cig/software/burnman/> Cottaar et al., 2014).

3.2. The anhydrous melt model

175 Thermodynamic models of MgO-SiO₂ melts are currently in their infancy. Many of the techniques used to constrain the thermodynamic properties (particularly the equations of state) of solids cannot be used on liquids as a result of their highly dynamic behaviour. Therefore in this study, we use MgO and SiO₂ melt models derived from molecular dynamics simulations (de Koker et al.,
180 2013), and fit a simplified mixing curve based on experimental data. First, however, the thermodynamic properties of the endmember melts need to be adjusted to fit the experimentally derived thermodynamic data at the melting point. This step was unnecessary in the original study of de Koker et al. (2013) because solid properties were also obtained by molecular dynamics simulations.
185 Such simulations do not provide good estimates of absolute energies and entropies, and so the values of the solids were obtained by fixing the melting point at a given pressure to the experimentally derived values (0 GPa, 3070 K for periclase, 14 GPa, 3120 K for stishovite). It turns out that the MD-determined entropy of periclase is almost identical to the experimentally determined values
190 at all pressures and temperatures (Stixrude and Lithgow-Bertelloni, 2011), so we only needed to adjust the standard state free energy. This leads to a periclase melting point of ~ 4180 K at 13 GPa, similar to that determined by previous ab-initio studies (Alfè, 2005). We notes that experimental results vary by about 1000 K about this value (3100 – 5373 K at 13 GPa Zerr and Boehler, 1994;
195 Zhang and Fei, 2008). Current thermodynamic models for periclase cannot be extrapolated to the extreme temperatures predicted by the Zhang and Fei (2008) data. However, assuming that the volume change of melting is roughly constant with temperature (1.8 cm³/mol at 13 GPa), the entropy of melting at a melting point of 5373 K would be about 50% of that for a melting point of
200 4180 K (13.25 vs. 27.5 J/K/mol). At 13 GPa and 2000 K, MgO melt would actually be 15 kJ/mol *more* stable as a result of this lower entropy.

The MD-determined entropy of stishovite is significantly lower than the ex-
 perimentally determined value, so we increased the standard state entropy of
 the melt by 16.5 J/K/mol. Conveniently, we also have a way to test the vol-
 205 umes predicted by the model of de Koker et al. (2013) at around 13 GPa. The
 experimentally-derived slope of the coesite melting curve is essentially zero at
 the triple point with stishovite at 13.7 GPa (Zhang et al., 1993). Therefore, from
 the Clausius-Clapeyron relationship $dT/dP = \Delta V/\Delta S$ the volumes of coesite
 and SiO₂ melt must be zero at this point. Unfortunately, the MD-derived SiO₂
 210 melt model has its density crossover with coesite about 4 GPa lower. Therefore,
 we adjusted the bulk modulus and reference pressure so satisfy this constraint,
 and the volume at zero pressure. The adjustments required here may not be a
 failing of the MD simulations; it is likely that the coordination changes in the
 SiO₂ melt require a higher order Birch Murnaghan EoS than that used by (de
 215 Koker et al., 2013). Our adjusted model is probably only accurate in a range of
 about ± 5 GPa around the triple point. The experimental data can also be used
 to judge the accuracy of the entropy of the SiO₂ melt model. The MD-derived
 entropy of melting is ~ 40 J/K/mol at the triple point. This value is in perfect
 agreement with the value derived from the Clapeyron slope of the stishovite
 220 liquidus (Shen and Lazor, 1995). We note that the slope recently proposed by
 Millot et al. (2015) is much shallower, but their slope is a two parameter Si-
 mon’s equation fit based on the triple point temperature at 13.7 GPa and the
 melting point at 500 GPa, and fits the data at 15–100 GPa (Shen and Lazor,
 1995; Lyzenga et al., 1983) rather poorly. A Simon’s equation fit is probably
 225 inappropriate over such extreme pressure ranges, especially where the melting
 point may be rather sensitive to changes in cation coordination.

A subregular solution model was adopted to describe the free energy of
 intermediate-composition MgO-SiO₂ melts. The two interaction parameters
 W_{MS} and W_{SM} at 14 GPa were derived from the melt composition at the
 230 forsterite (fo)-HP clinoenstatite (hen) eutectic (Presnall et al., 1998) and melt-
 ing temperatures at the fo, hen and fo-hen cotectic compositions (Presnall and
 Gasparik, 1990; Presnall and Walter, 1993). We assumed an ideal entropic con-

tribution to mixing. The pressure dependencies were fit to the melting curves. It should be noted that although the excess volumes are similar to the results of de Koker et al. (2013), the excess entropies are some 50% lower. However, they provide an excellent fit to the forsterite and orthoenstatite melting curves (see Supplementary Materials).

3.3. The hydrous melt model

In this study, the anhydrous components in our hydrous melts are normalised to a one-cation basis (i.e. MgO, $\text{Mg}_{2/3}\text{Si}_{1/3}\text{O}_{4/3}$, $\text{Mg}_{1/2}\text{Si}_{1/2}\text{O}_{3/2}$, SiO_2). We follow Silver and Stolper (1985) in determining the proportions of $\text{H}_2\text{O} + \text{O}_{br}$ and OH_{tm} in the melt as a function of the molar proportion of H_2O $p_{\text{H}_2\text{O}}$ as follows:

$$p' = \frac{p_{\text{H}_2\text{O}}}{p_{\text{H}_2\text{O}} + r(1 - p_{\text{H}_2\text{O}})} \quad (6)$$

$$X_{\text{O}} = 1 - p' - \frac{0.5 - \sqrt{0.25 - \frac{K_{(1)}-4}{K_{(1)}}(p' - p'^2)}}{\frac{K_{(1)}-4}{K_{(1)}}} \quad (7)$$

$$X_{\text{H}_2\text{O}} = X_{\text{O}} + 2p' - 1 \quad (8)$$

$$X_{\text{OH}} = 1 - X_{\text{O}} - X_{\text{H}_2\text{O}} \quad (9)$$

p' is the molar proportion of H_2O where the silicate is normalised on a one oxygen basis (rather than a one-cation basis). We assume that all bridging oxygens are equally likely to be protonated. The number of oxygens per formula unit r thus increases monotonously from 1 to 2 across the MgO-SiO₂ binary ($r_{\text{per}} = 1$, $r_{\text{fo, wad, rw}} = 4/3$, $r_{\text{oen, cen}} = 3/2$, and $r_{\text{coe, stv}} = 2$). The ideal activities of the anhydrous and water components can then be calculated:

$$a_{\text{ideal melt}}^{\text{s}} = X_{\text{O}}^r \quad (10)$$

$$a_{\text{ideal melt}}^{\text{H}_2\text{O}} = X_{\text{H}_2\text{O}} \quad (11)$$

The activity coefficients (i.e. the activity prefactor which provides the non-ideal contribution to mixing; $a = \gamma a_{\text{ideal}}$) are equal to one except in the case

of the MgO-H₂O binary, where a simple Margules model is applied (Hunt and Manning, 2012)

$$RT \ln \gamma_i = p_j^2 (1 - p_j) (2W_{ji} - W_{ij}) \quad (12)$$

where the subscripts i and j correspond to the components s or H₂O. Equilibrium with the solid can now be found using Equation 5, noting that the dataset-derived values of G_{solid}^s of the forsterite (Mg₂SiO₄) and enstatite (Mg₂Si₂O₆) polymorphs should be divided by 3 and 4 to reduce them to their one-cation equivalents.

4. Results

260 4.1. *Ex-situ observations*

Experimental details and results are shown in Table 2. Superliquidus runs revealed networks of dendritic crystals of brucite, forsterite, enstatite and stishovite. Below the liquidus, solid phases tended to aggregate at the cold end of the capsules. Periclase formed equant crystals often associated with quench over-
265 growths which appear brighter in BSE images. Forsterite formed tabular crystals about 100 μm long. Enstatite crystals were much smaller, forming ca. 5 μm equant grains. Stishovite also formed equant to blocky grains, but crystals only separated from the melts in chambers with a high water content. In addition to the difference in texture and shape between quench crystals liquidus phases, subliquidus phases typically contained many small inclusions of Pt-Rh oxides.
270 A typical set of run products is shown in Figure 2.

Figure 1: The 18/11 octahedral assembly design used in this study.

Table 2: Experimental run conditions and run products determined by SEM/EDS. Compositions are listed in order of increasing molar H₂O content. Unused compositions for each run are marked by an en-dash. Minor solids are listed in brackets. Mineral abbreviations are as follows: br - brucite, per - periclase, co - hydroxychondrodite, en - clinoenstatite, s - stishovite.

Expt #	P (GPa)	T (°C)	t (min)	brucite+PtAc	forsterite+PtAc	enstatite+PtAc	quartz+PtAc	br+q
Z1063	13	1200	40	-/br/br/br/L	co/fo/fo/(fo)	en/en/en/en	-/-/-/-/-/-/-	-/-/-/-
Z1085	13	1300	40	-/-/per/L/L	-/fo/(en)/L	-/-/-/-	-/-/-/-/-/-/-	-/-/-/-
Z1079	13	1300	35	-/per/per/L/L	fo/fo/en/(en)	en/en/en/en	-/-/-/-/-/-/-	-/-/-/-
Z1058	13	1400	30	-/per/(per)/L/L	fo/(fo)/L/L	en/en/en/(en)	-/-/-/-/-/-/-	-/-/-/-
Z1060	13	1500	20	-/-/-/-/-	(fo)/L/L/L	en/en/L/L	-/-/-/-/-/-/-	-/-/-/-
Z1140	13	1600	10	-/-/-/-/-	-/-/-/-	-/-/-/-	s/s/s/s/s/s/(s)	s+en/en/en/en
Z1084	13	1650	10	-/-/-/-/-	-/-/-/-	L/L/-/-	-/-/-/-/-/-/-	-/-/-/-
Z1207	13	1700	8	-/-/-/-/-	-/-/-/-	-/-/-/-	s/s/s/s/s/s/(s)/L	s+en/(en)/L/L
Z1209	13	1800	5	-/-/-/-/-	-/-/-/-	-/-/-/-	s/s/s/s/(s?)/L/L/L	s/L/L/L
Z1091	13	1900	5	(per)/-/-/-/-	-/-/-/-	-/-/-/-	-/-/-/L/-/L/L/L	L/L/-/-

Figure 2: BSE image of typical run products. Experimental chambers from Experiment Z1058, conducted at 1400 °C and 13 GPa. Chambers have compositions along the forsterite-water binary, with water contents increasing from left to right.

4.2. Subsystems

4.2.1. $MgO-H_2O$

Experimental results for the system $MgO-H_2O$ are shown in Figure 3. The
 275 periclase-brucite-water invariant at 13 GPa is well constrained at 62–66 mol%
 H_2O and ~ 1200 °C. The MgO content of the fluid increases gradually with
 increasing pressure, as a result of the extremely high melting temperature of
 periclase. In addition to the thermodynamic models described in the methods
 section, the activity of H_2O at the brucite-periclase-melt triple point is calcu-
 280 lated using the thermodynamic dataset of (Holland and Powell, 2011), which
 includes models for brucite, periclase and water (Pitzer and Sterner, 1995). This
 provides an additional constraint on the melt model via the equation

$$RT \ln a_{H_2O} = G_{br} - G_{per} - G_{H_2O} \quad (13)$$

The brucite melting curve is obtained by finding the solution to the equation

$$(G_{MgO,melt} + RT \ln a_{MgO}) + (G_{H_2O,HP} + RT \ln a_{H_2O}) = G_{br,HP} - G_{per,HP} + G_{per,SLB} \quad (14)$$

where the right hand side is the chemical potential of $Mg(OH)_2$ in the melt,
 285 and the right hand side is the Gibbs free energy of brucite with a correc-
 tion for the different standard state energies of MgO between the Holland and
 Powell (2011) and Stixrude and Lithgow-Bertelloni (2011) datasets. $G_{(1)} =$
 $RT \ln K_{(1)} = -75000$ J/mol ($r=1$) provides a good fit to the data if additional
 asymmetry is added via a binary subregular model ($W_{MgO-H_2O} = 55000$ J/mol,
 290 $W_{H_2O-MgO} = 0$ J/mol). The large positive interaction parameter increases the
 tendency for melt-fluid immiscibility at the water-rich end of the system. This
 is reflected in the flat slope of the brucite liquidus, and is in excellent agreement

Figure 3: The periclase-water phase diagram at 13 GPa, based on current experimental results. Model fits to the data use the melt formulation of Silver and Stolper (1985), with $r=1$ and $K=K(T)$ (see discussion in main text). Properties of the anhydrous solid and melt are taken from published literature (Stixrude and Lithgow-Bertelloni, 2011; de Koker et al., 2013). An additional subregular interaction term is required to match the composition and temperature of brucite dehydration.

with the suggestion that the second critical endpoint in the $\text{MgO-H}_2\text{O}$ system probably lies at ca. 12–13 GPa (Melekhova et al., 2007).

295 The dehydration of brucite at high pressure was previously studied by Fukui et al. (2005). They reported that the stability of brucite reaches a maximum at about 9–10 GPa and 1200 °C, decomposing at 1100–1150 °C at 13 GPa. The temperature difference between their study and ours is therefore 50 °C, within experimental uncertainties.

300 4.2.2. Mg_2SiO_4 - H_2O

The melting point depression of forsterite in the presence of water at 13 GPa is illustrated in Figure 4. The model parameters shown are $G_{(1)} = 75 \cdot (1420 - T)$ J/mol, $r = 4/3$. The anhydrous melting of forsterite is incongruent, so the high temperature part of the liquidus is metastable with respect to a
 305 mixture of periclase and liquid (see also Figure 7). Water-rich chambers from experiments run at 1300 °C revealed small quantities of enstatite, indicating that the forsterite-enstatite cotectic crosses the Mg_2SiO_4 - H_2O tie line at 1300-1400 °C. This is in excellent agreement with results on the wadsleyite-water system run at 15 GPa (Demouchy et al., 2005; Litasov et al., 2011). At 1200
 310 °C, one chamber contained large crystals of hydroxychondrodite. The presence of this MgO-rich phase in the chamber with the lowest water contents may be explained an MgO-deficit in forsterite resulting from the incorporation of hydrogen via the substitution mechanism $Mg^{2+} \rightarrow 2H^+$ (Keppler and Bolfan-Casanova, 2006). Alternatively it could simply be the result of a small SiO_2
 315 deficit in that sample chamber.

Figure 4: The forsterite-water phase diagram at 13 GPa, based on current experimental results. The thermodynamics of pure forsterite are taken from the literature (Stixrude and Lithgow-Bertelloni, 2011), and the properties of the anhydrous melt are from the mixing model described in the text. At high temperatures, the forsterite liquidus is metastable with respect to periclase + melt. High temperature data come from the study of Novella et al. (2015).

4.2.3. $MgSiO_3$ - H_2O

The melting of high pressure clinoenstatite in the presence of water is shown in Figure 5. Unlike the forsterite or periclase liquids, the observed depression of melting at low water contents exceeds that predicted by even the most extreme
320 commonly-used ideal mixing model, where all oxygens in the melt are equivalent and available for protonation, and molecular H_2O is absent (Silver and Stolper, 1985). The liquidus at higher water contents can be fit well with model parameters $G_{(1)} = 120 \cdot (1750 - T)$ J/mol, $r = 3/2$. The disagreement between this model and the experimental observations is small, and could plausibly be due
325 to experimental error. However, given the results for stishovite (see next section), we feel that more complex models are required to explain the depression of melting in the $MgSiO_3$ system.

Figure 5: The clinoenstatite-water phase diagram at 13 GPa, based on current experimental results. The thermodynamics of pure high pressure clinoenstatite are taken from the literature (Stixrude and Lithgow-Bertelloni, 2011), and the properties of the anhydrous melt are from the mixing model described in the text. High temperature data come from the study of Novella et al. (2015).

Our experimentally determined liquidus is in excellent agreement with the experimental results of Yamada et al. (2004), as is the absence of stishovite in
330 any of the sample chambers. We note that although we do not have any evidence for melt-fluid immiscibility, the flat liquidus at ca. 1500 °C causes a very rapid change from water-rich to water-poor fluids with increasing temperature, in agreement with Inoue (1994) and Yamada et al. (2004). The implication is that for a given bulk H_2O content, a sharp rise in the degree of partial melting will
335 occur at about 1500 °C in hydrous $MgSiO_3$ melts.

4.2.4. $\text{SiO}_2\text{-H}_2\text{O}$

The 13 GPa $\text{SiO}_2\text{-H}_2\text{O}$ binary phase diagram is shown in Figure 6. While the deviation between the predicted enstatite liquidus depression for ideal molecular H_2O -free melts and the experimental observations are relatively small, the deviation for the stishovite data is extreme. The mixing model presented in Figure 6 has parameters $G_{(1)} = 100 \cdot (1200 - T)$ J/mol, $r = 2$ is fit to the extrapolation of the experimentally defined liquidus, but clearly fails to fit any of the experimental data. There are several possible explanations for this. First, the melting point of anhydrous stishovite (which is metastable with respect to coesite) could be overestimated by ca. 300 °C, or the entropy of melting could be 10–20 J/K/mol, rather than 40 J/K/mol. Neither of these possibilities is very likely; the coesite and stishovite melting curves provide good constraints on the volume and entropy of SiO_2 melt in the region of the triple point at ca. 13.5 GPa. A third possibility is that approximately 30% volume liquidus-phase stishovite crystals were missed during SEM analysis. This is also extremely unlikely; the equant and dendritic morphologies of liquidus and quench stishovite are instantly recognisable, and the thermal gradients in the capsule lead to melt separation on the timescales of the experiments, such that even a small (5%) volume proportion of solids should be detected.

Figure 6: The silica-water phase diagram at 13 GPa, based on current experimental results. The thermodynamics of stishovite and the anhydrous melt are described in the text. At high temperatures, the stishovite liquidus is metastable with respect to coesite and melt.

Having ruled out experimental error and uncertainties in the thermodynamics of the anhydrous system, the only possibility is that hydrous SiO_2 melts with relatively low water contents are stabilised well beyond the expected entropic stabilisation from random protonation of the silica network. The causes of this additional stability (and, to a lesser extent, that of hydrous MgSiO_3 melts) are well beyond the scope of the current study, but may be a fruitful line of investigation for molecular dynamics simulations (e.g. Karki and Stixrude, 2010).

4.3. The $MgO-SiO_2-H_2O$ system

The set of experimental analyses can be used to create a preliminary ternary liquidus diagram (Figure 7). It should be noted that the periclase liquidus field and periclase-forsterite cotectic are poorly constrained by the data. The low temperature extension of the cotectic is chosen to fit the reported Mg:Si ratios of melts in equilibrium with forsterite and various DHMS phases at 13.5 GPa (Melekhova et al., 2007).

Figure 7: A preliminary ternary liquidus diagram at 13 GPa, based on current experimental results. Contours are in $^{\circ}C$, and mineral abbreviations are liquidus fields as follows: per - periclase, fo - forsterite, en - clinoenstatite, stv - stishovite, coe - coesite, phB - phase B, br - brucite, chond - hydroxchondrodite, ice - ice VII.

5. Discussion

5.1. Melting in deep subduction zones and atop the mantle transition zone

Our melt model in the MSH system serves as a useful tool for investigating melting at high pressures in the mantle. In particular, the forsterite-enstatite cotectic implies that hydrous melts in equilibrium with depleted peridotites at typical mantle temperatures of 1500 $^{\circ}C$ will contain ~ 48 mol% H_2O and an Mg:Si ratio of about 2 (the same as forsterite), corresponding to about 26 wt% H_2O . Such compositions are far too water-rich to be neutrally buoyant relative to a forsterite + enstatite assemblage (Mookherjee et al., 2008), and will rise through the mantle. Adding further components to the system will modify this behaviour. In particular, the addition of iron lowers anhydrous melting temperatures and increases melt densities. Thus, we cannot directly use our results to confirm or refute the viability of the water-filter model proposed by Bercovici and Karato (2003), which requires neutrally buoyant or dense melts at the 410 km discontinuity. However, the flat liquidus curves revealed by our experiments are likely to also be observed in more natural chemical systems. The current results imply that the water contents of melts in equilibrium with

forsterite and enstatite drop from 62 mol% (34 wt%) to around 30 mol% (16 wt%) between 1300 and 1700 °C. For a given water content, this rapid change in composition must be balanced by a rapid increase in the mass fraction of partial melt, which could greatly enhance chances of detection by seismological or other geophysical techniques. Such large decreases in water content would also lead to large density changes; close to slabs, hydrous melts could be buoyant, while in warmer mantle of a similar composition they would be dense. This scenario might be expected to result in channelisation of hydrous melts close to the top interface of subducting slabs. Finally, large decreases in water contents are also likely to have a profound effect on melt viscosity, and may encourage reaction-infiltration instabilities encouraging melt channelisation (Spiegelman et al., 2001).

5.2. Water partitioning in the mantle transition zone

Partitioning of hydrogen between mineral and melt phases can be described using a partition coefficient D:

$$D_{H_2O}^{a/b} = c_{H_2O}^a / c_{H_2O}^b \quad (15)$$

where $c_{H_2O}^i$ is the concentration of H₂O (in wt%) in phase i (Keppler and Bolfan-Casanova, 2006). In quenchable phases, there are a number of ways that concentration can be measured, including FTIR, SIMS and ERDA. In the case of melts, which are unquenchable, $c_{H_2O}^{melt}$ in partitioning studies has most commonly been estimated by mass balance or by assuming that the deficit in microprobe totals is due to hydrogen. In two studies on Fe-free wadsleyite, Demouchy et al. (2005) and Litasov et al. (2011) present estimates of water content in melts calculated from microprobe deficits. A similar study on ringwoodite was undertaken by Ohtani et al. (2000). The T- X_{H_2O} dependencies of the melts in equilibrium with wadsleyite or ringwoodite are strikingly different (Figure 8). For example, melt in equilibrium with wadsleyite at 15 GPa and 1400 °C was estimated to contain 10.6-13.3 wt% H₂O, while melt compositions in equilibrium with ringwoodite at 20 GPa and 1400 °C suggest water contents of 57-66 wt%

415 H₂O. Modelled Mg₂SiO₄ melting temperatures increase by only 40 K between
15 and 20 GPa, and entropies of melting at these two pressures are not very
different (92.4 vs. 97 J/K/mol), so unless the thermodynamics of mixing in
the liquid change markedly between these pressures, estimates of $c_{H_2O}^{melt}$ for the
ringwoodite or wadsleyite studies (or both) must be somewhat inaccurate. We
420 note that two of the three melt compositions in equilibrium with ringwoodite fall
above the temperatures indicating that hydrogen exists only as molecular H₂O
(Silver and Stolper, 1985). In addition, the calculated liquidus temperatures
in the wadsleyite studies at 15 GPa are lower than those reported at 5.5 GPa
(Inoue, 1994). Both of these observations appear highly unlikely.

425 Here, we recalculate the wadsleyite/melt and ringwoodite/melt partitioning
values with our melt model, assuming that our fitted values of $G_{(1)}$ and r are
suitable between 13 and 20 GPa. We justify this by noting that speciation is
likely to be only weakly dependent on pressure under these conditions. Water
concentrations in the solid are taken from the original studies. We restrict our
430 analysis to data from 1100–1400 °C, where the Mg:Si ratios of the melts are
similar to that in forsterite. At 15 GPa, $D_{H_2O}^{wad/melt}$ increases from 0.30 to 0.51
between 900 and 1200 °C, and then decreases back to 0.32 at 1400 °C. The three
ringwoodite H₂O concentrations (20–23 GPa) indicate a decrease in $D_{H_2O}^{rw/melt}$
from 0.68 to 0.57 between 1300 and ca. 1400 °C.

Figure 8: Water concentrations in wadsleyite, ringwoodite and melt, modelled at 15 and 20
GPa. Experimental data is taken from three published studies (Ohtani et al., 2000; Demouchy
et al., 2005; Litasov et al., 2011).

435 We now create thermodynamic models for incorporation of H₂O into forsterite,
wadsleyite and ringwoodite. For forsterite, we use high pressure (12–14 GPa)
experimental data on the solids from Smyth et al. (2006) and Litasov et al.
(2009); neither of these studies estimate coexisting melt compositions. Hydro-
gen in all three minerals is incorporated as proton pairs substituting for Mg
440 ($Mg^{2+} \leftrightarrow 2H^+$) (Smyth, 1987; Smyth et al., 2003). Ringwoodite potentially
also exhibits a substitution involving Si ($Si^{4+} \leftrightarrow Mg^{2+} + 2H^+$) (Kudoh et al.,

2000). Both of these reactions may be written in the form



which leads to the equilibrium relation

$$\Delta G = -RT \ln \left(\frac{a_{(OH)_2}}{a_{H_2O} a_O} \right), \quad (17)$$

$$= \Delta H - (T - T_0)\Delta S + (P - P_0)\Delta V \quad (18)$$

where ΔG is the Gibbs energy associated with the reaction. The second equation
 445 is a linearised form of the expression describing the change in free energy with
 pressure and temperature. The first equation can be simplified by making the
 approximation that a_O is constant and that the weight percentage of H_2O in the
 solid c_{H_2O} is proportional to the activity of $(OH)_2$. Both of these assumptions
 are probably reasonable at low values of c_{H_2O} . Rearranging now produces the
 450 expression:

$$c_{H_2O} \propto a_{H_2O} \exp \left(-\frac{\Delta H - (T - T_0)\Delta S + (P - P_0)\Delta V}{RT} \right) \quad (19)$$

Further simplifications can be made by taking $T_0 = 0$ K, by realising that
 P_0 can be neglected at high pressures, and by incorporating the factor $\Delta S/R$
 into the exponential prefactor. Finally, it is recognised that the pressure and
 temperature dependence of the Gibbs free energy of water G_{H_2O} is highly non-
 455 linear. For this reason, we split the Gibbs free energy change of the anhydrous
 and hydrous solid from that of the liquid, yielding the equation (Keppler and
 Bolfan-Casanova, 2006):

$$c_{H_2O} = A a_{H_2O} f_{H_2O} \exp \left(-\frac{\Delta H + P\Delta V^{solid}}{RT} \right), \quad (20)$$

$$f_{H_2O} = \exp \left(\frac{\Delta G_{H_2O}}{RT} \right) \quad (21)$$

We calculate the fugacity of pure water f_{H_2O} from the equation of state
 of (Pitzer and Sterner, 1995). We can now fit the values of A , ΔH and ΔV
 460 to the experimental data on forsterite, wadsleyite and ringwoodite using our
 melt model to provide estimates of a_{H_2O} . The sharp spike in olivine water

Table 3: Thermodynamic models for water solubility in wadsleyite and ringwoodite

Phase	P_{ref} (Pa)	A [kg/(kgPa)]	$\Delta H_{P_{ref}}$ [J/mol]	ΔV [m ³ /mol]
Olivine	1.2e10	3.23e-12	1.50e5	1e-5
Wadsleyite	1.5e10	1.97e-12	1.60e5	1e-5
Ringwoodite	2.0e10	1.46e-12	2.03e5	1e-5 (fixed)

concentrations at 1250 °C reported by Smyth et al. (2006) is difficult to fit with reasonable enthalpies, but we obtain good fits with the rest of their data, and those of Litasov et al. (2009). The wadsleyite data of Demouchy et al. (2005) at 1200 °C and 14–17 GPa are consistent with a low pressure effect on water content, implying that $\Delta V \sim 10^{-5}$ m³/mol, similar or slightly lower than estimates for olivine ($1.00 - 1.06 \cdot 10^{-5}$ m³/mol Kohlstedt et al., 1996; Zhao et al., 2004; Mosenfelder et al., 2006). A single data point at 18 GPa has much lower water contents, which would require $\Delta V \sim 1.25 \cdot 10^{-5}$ m³/mol. This value is inconsistent with the large water contents at 16 and 17 GPa, and is probably unreasonable given the reported values for olivine. We therefore favour the lower estimate of ΔV , and assume the same value for ringwoodite. The model values are shown in Table 3.

These models allow us to predict the partition coefficients of water between olivine, wadsleyite and melt at the 410 km discontinuity (~ 14 GPa; Figure 10), and wadsleyite, ringwoodite and melt at the 520 km discontinuity (~ 18 GPa; Figure 10). $D_{H_2O}^{wad/fo}$ displays a decrease from ~ 4 at 1000 °C to ~ 1.8 at 2000 °C, in good agreement with the estimates of Litasov et al. (2011) at low temperatures, but without a return to high values at high temperatures, where water contents are lower and prone to large relative errors. $D_{H_2O}^{ring/wad}$ decreases from ~ 1.4 at 1000 °C to ~ 1.1 at 2000 °C. These values imply that upwelling across both the 410 and the 520 km discontinuity will cause partial melting. Both boundaries have been associated with low seismic velocities, which may indicate zones of deep melting (e.g. Jasinsek et al., 2010). The small temperature dependence on the wadsleyite-ringwoodite partition coefficient implies that

repartitioning of water during secular cooling within the mantle transition zone is likely to be more minor (and in the opposite direction) to that proposed by Demouchy et al. (2005).

Figure 9: Modelled partition coefficient between forsterite, wadsleyite and melt at 14 GPa, approximately the pressure of the 410 km discontinuity. Note the separate scales for solid/solid and solid/melt partitioning. The difference in melt compositions between this study and that of Demouchy et al. (2005) results in much lower $D^{wad/melt}$ coefficients. Error bars on the wadsleyite datapoints are those reported by Demouchy et al. (2005).

Figure 10: Modelled partition coefficient between wadsleyite, ringwoodite and melt at 18 GPa, approximately the pressure of the 520 km discontinuity. Note the separate scales for solid/solid and solid/melt partitioning. Error bars on the ringwoodite data points indicate the range of values reported by Ohtani et al. (2000). Error bars on the wadsleyite data points indicate 1 s.d. uncertainties as reported by Litasov et al. (2011).

6. Acknowledgements

490 The authors would like to thank Gerti Gollner for acquiring capsule materials, Stefan Übelhack and Heinz Fischer for assembly and capsule cutting and Hubert Schulze for sample preparation. RM was supported by a Humboldt Postdoctoral Fellowship. This study was funded by the ACCRETE project (European Research Council Advanced Grant, contract number 290568).

495 **References**

- Alfè, D., 2005. Melting Curve of MgO from First-Principles Simulations. *Physical Review Letters* 94, 235701.
- Bercovici, D., Karato, S.i., 2003. Whole-mantle convection and the transition-zone water filter. *Nature* 425, 39–44.
- 500 Cottaar, S., Heister, T., Rose, I., Unterborn, C., 2014. BurnMan: A lower mantle mineral physics toolkit. *Geochemistry, Geophysics, Geosystems* 15, 1164–1179.
- de Koker, N., Karki, B.B., Stixrude, L., 2013. Thermodynamics of the MgO-SiO₂ liquid system in Earth’s lowermost mantle from first principles. *Earth and Planetary Science Letters* 361, 58–63.
- 505 Demouchy, S., Deloule, E., Frost, D.J., Keppler, H., 2005. Pressure and temperature-dependence of water solubility in Fe-free wadsleyite. *American Mineralogist* 90, 1084–1091.
- Frost, D.J., Poe, B.T., Trønnes, R.G., Liebske, C., Duba, A., Rubie, D.C., 2004. A new large-volume multianvil system. *Physics of the Earth and Planetary Interiors* 143, 507–514.
- 510 Fukui, H., Inoue, T., Yasui, T., Katsura, T., Funakoshi, K.i., Ohtaka, O., 2005. Decomposition of brucite up to 20 GPa: evidence for high MgO-solubility in the liquid phase. *European Journal of Mineralogy* 17, 261–267.
- Holland, T.J.B., Powell, R., 2011. An improved and extended internally consistent thermodynamic dataset for phases of petrological interest, involving a new equation of state for solids. *Journal of Metamorphic Geology* 29, 333–383.
- 515 Hunt, J.D., Manning, C.E., 2012. A thermodynamic model for the system SiO₂-H₂O near the upper critical end point based on quartz solubility experiments at 500–1100 °C and 5–20 kbar. *Geochemica and Cosmochemica Acta* 86, 196–213.
- 520

- Inoue, T., 1994. Effect of water on melting phase relations and melt composition in the system $\text{Mg}_2\text{SiO}_4\text{--MgSiO}_3\text{--H}_2\text{O}$ up to 15 GPa. *Physics of the Earth and Planetary Interiors* 85, 237–263.
- 525 Jasbinsek, J.J., Dueker, K.G., Hansen, S.M., 2010. Characterizing the 410 km discontinuity low-velocity layer beneath the LA RISTRA array in the North American Southwest. *Geochemistry, Geophysics, Geosystems* 11, n/a–n/a. Q03008.
- Karki, B.B., Stixrude, L., 2010. First-Principles Study of Enhancement of Trans-
530 port Properties of Silica Melt by Water. *Physical Review Letters* 104, 215901.
- Keppler, H., Bolfan-Casanova, N., 2006. Thermodynamics of water solubility and partitioning. *Reviews in Mineralogy and Geochemistry* 62, 193–230.
- Keppler, H., Frost, D.J., 2005. Introduction to minerals under extreme conditions, in: Miletich, R. (Ed.), *Mineral Behaviour at Extreme Conditions*. EMU. volume 7 of *European Mineralogical Union Lecture Notes in Mineralogy*, pp.
535 1–30.
- Kohlstedt, D.L., Keppler, H., Rubie, D.C., 1996. Solubility of water in the α , β and γ phases of $(\text{Mg,Fe})_2\text{SiO}_4$. *Contributions to Mineralogy and Petrology* 123, 345–357.
- 540 Komabayashi, T., Omori, S., Maruyama, S., 2005. Experimental and theoretical study of stability of dense hydrous magnesium silicates in the deep upper mantle. *Physics of the Earth and Planetary Interiors* 153, 191209.
- Kudoh, Y., Kuribayashi, T., Mizobata, H., Ohtani, E., 2000. Structure and cation disorder of hydrous ringwoodite, $\gamma\text{-Mg}_{1.89}\text{Si}_{0.98}\text{H}_{0.30}\text{O}_4$. *Physics and*
545 *Chemistry of Minerals* 27, 474–479.
- Litasov, K.D., Shatskiy, A., Ohtani, E., Katsura, T., 2011. Systematic study of hydrogen incorporation into Fe-free wadsleyite. *Physics and Chemistry of Minerals* 38, 75–84.

- 550 Litasov, K.D., Shatskiy, A.F., Katsura, T., Ohtani, E., 2009. Water solubility
in forsterite at 8-14 GPa. *Doklady Earth Sciences* 425, 432–435.
- Lyzenga, G.A., Ahrens, T.J., Mitchell, A.C., 1983. Shock temperatures of SiO_2
and their geophysical implications. *Journal of Geophysical Research* 88, 2431–
2444.
- 555 Melekhova, E., Schmidt, M.W., Ulmer, P., Pettke, T., 2007. The composition
of liquids coexisting with dense hydrous magnesium silicates at 11–13.5 GPa
and the endpoints of the solidi in the $\text{MgO-SiO}_2\text{-H}_2\text{O}$ system. *Geochemica*
and *Cosmochemica Acta* 71, 3348–3360.
- 560 Millot, M., Dubrovinskaia, N., Černok, A., Blaha, S., Dubrovinsky, L., Braun,
D.G., Celliers, P.M., Collins, G.W., Eggert, J.H., Jeanloz, R., 2015. Shock
compression of stishovite and melting of silica at planetary interior conditions.
Science 347, 418–420.
- Mookherjee, M., Stixrude, L., Karki, B., 2008. Hydrous silicate melt at high
pressure. *Nature* 452, 983–986.
- 565 Mosenfelder, J.L., Deligne, N.I., Asimow, P.D., Rossman, G.R., 2006. Hydrogen
incorporation in olivine from 2–12 GPa. *American Mineralogist* 91, 285–294.
- Nagano, Y., 2002. Standard enthalpy of formation of platinic acid. *The Journal*
of *Chemical Thermodynamics* 34, 1745–1750.
- Novella, D., Dolejs, D., Myhill, R., Frost, D.J., 2015. Melting phase relations in
the systems $\text{Mg}_2\text{SiO}_4\text{-H}_2\text{O}$ and $\text{MgSiO}_3\text{-H}_2\text{O}$ at upper mantle conditions. in
570 prep .
- Ohtani, E., Mizobata, H., Yurimoto, H., 2000. Stability of dense hydrous mag-
nesium silicate phases in the systems $\text{Mg}_2\text{SiO}_4\text{-H}_2\text{O}$ and $\text{MgSiO}_3\text{-H}_2\text{O}$ at
pressures up to 27 GPa. *Physics and Chemistry of Minerals* 27, 533–544.
- 575 Pearson, D.G., Brenker, F.E., Nestola, F., McNeill, J., Nasdala, L., Hutchison,
M.T., Matveev, S., Mather, K., Silversmit, G., Schmitz, S., Vekemans, B.,

Vincze, L., 2014. Hydrous mantle transition zone indicated by ringwoodite included within diamond. *Nature* 507, 221–224.

Pitzer, K., Sterner, S., 1995. Equations of state valid continuously from zero to extreme pressures with H₂O and CO₂ as examples. *International Journal of Thermophysics* 16, 511–518.

Poli, S., Schmidt, M.W., 2002. Petrology of Subducted Slabs. *Annual Review of Earth and Planetary Sciences* 30, 207–235.

Presnall, D.C., Gasparik, T., 1990. Melting of enstatite (MgSiO₃) from 10 to 16.5 GPa and the forsterite (Mg₂SiO₄)-majorite (MgSiO₃) eutectic at 16.5 GPa: Implications for the origin of the mantle. *Journal of Geophysical Research: Solid Earth* 95, 15771–15777.

Presnall, D.C., Walter, M.J., 1993. Melting of forsterite, Mg₂SiO₄, from 9.7 to 16.5 GPa. *Journal of Geophysical Research* 98, 19777.

Presnall, D.C., Weng, Y.H., Milholland, C.S., Walter, M.J., 1998. Liquidus phase relations in the system MgO-MgSiO₃ at pressures up to 25 GPa: constraints on crystallization of a molten Hadean mantle. *Physics of the Earth and Planetary Interiors* 107, 83–95.

Shen, A., Keppler, H., 1995. Infrared spectroscopy of hydrous silicate melts to 1000 degrees C and 10 kbar; direct observation of H₂O speciation in a diamond-anvil cell. *American Mineralogist* 80, 1335–1338.

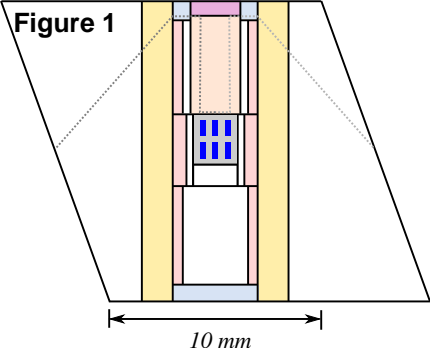
Shen, G., Lazor, P., 1995. Measurement of melting temperatures of some minerals under lower mantle pressures. *Journal of Geophysical Research* 100, 17699.

Silver, L., Stolper, E., 1985. A Thermodynamic Model for Hydrous Silicate Melts. *Journal of Geology* 93, 161–177.

Smyth, J.R., 1987. β -Mg₂SiO₄: a potential host for water in the mantle? *American Mineralogist* 72, 1051–1055.

- Smyth, J.R., Frost, D.J., Nestola, F., Holl, C.M., Bromiley, G., 2006. Olivine hydration in the deep upper mantle: Effects of temperature and silica activity. *Geophysical Research Letters* 33, 15301. L15301.
- 605 Smyth, J.R., Holl, C.M., Frost, D.J., Jacobsen, S.D., Langenhorst, F., McCammon, C.A., 2003. Structural systematics of hydrous ringwoodite and water in Earth's interior. *American Mineralogist* 88, 1402–1407.
- Spiegelman, M., Kelemen, P.B., Aharonov, E., 2001. Causes and consequences of flow organization during melt transport: The reaction infiltration instability in compactible media. *Journal of Geophysical Research* 106, 2061–2077.
- 610 Stixrude, L., Lithgow-Bertelloni, C., 2011. Thermodynamics of mantle minerals - II. Phase equilibria. *Geophysical Journal International* 184, 1180–1213.
- Stolper, E., 1982. The speciation of water in silicate melts. *Geochemica Cosmochemica Acta* 46, 2609–2620.
- 615 Tenner, T.J., Hirschmann, M.M., Humayun, M., 2012. The effect of H₂O on partial melting of garnet peridotite at 3.5 GPa. *Geochemistry, Geophysics, Geosystems* 13, 3016.
- Yamada, A., Inoue, T., Irifune, T., 2004. Melting of enstatite from 13 to 18 GPa under hydrous conditions. *Physics of the Earth and Planetary Interiors* 147, 4556.
- 620 Zerr, A., Boehler, R., 1994. Constraints on the melting temperature of the lower mantle from high-pressure experiments on MgO and magnesiowüstite. *Nature* 371, 506–508.
- Zhang, J., Liebermann, R.C., Gasparik, T., Herzberg, C.T., Fei, Y., 1993. Melting and subsolidus relations of SiO₂ at 9–14 GPa. *Journal of Geophysical Research: Solid Earth* 98, 19785–19793.
- 625 Zhang, L., Fei, Y., 2008. Melting behavior of (Mg,Fe)O solid solutions at high pressure. *Geophysical Research Letters* 35, 13302.

- ⁶³⁰ Zhao, Y.H., Ginsberg, S.B., Kohlstedt, D.L., 2004. Solubility of hydrogen in olivine: dependence on temperature and iron content. *Contributions to Mineralogy and Petrology* 147, 155–161.








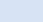



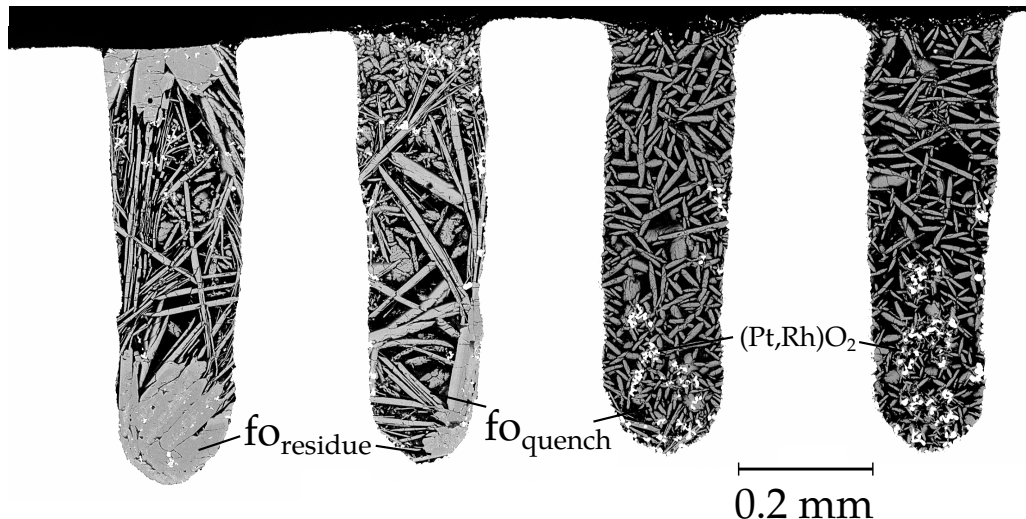
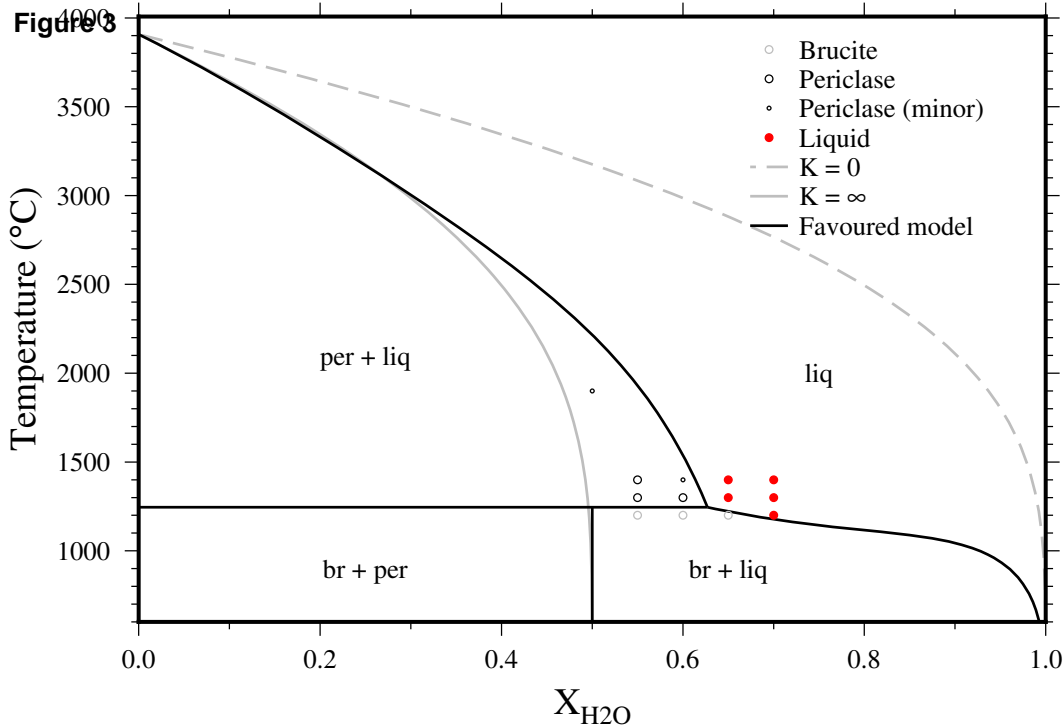
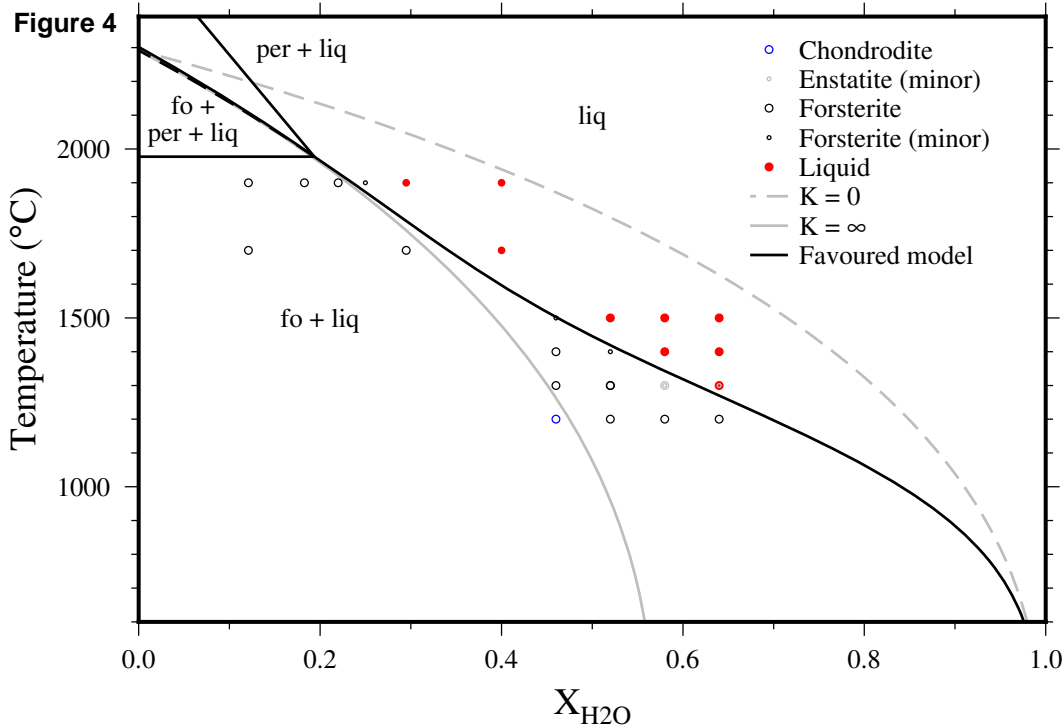
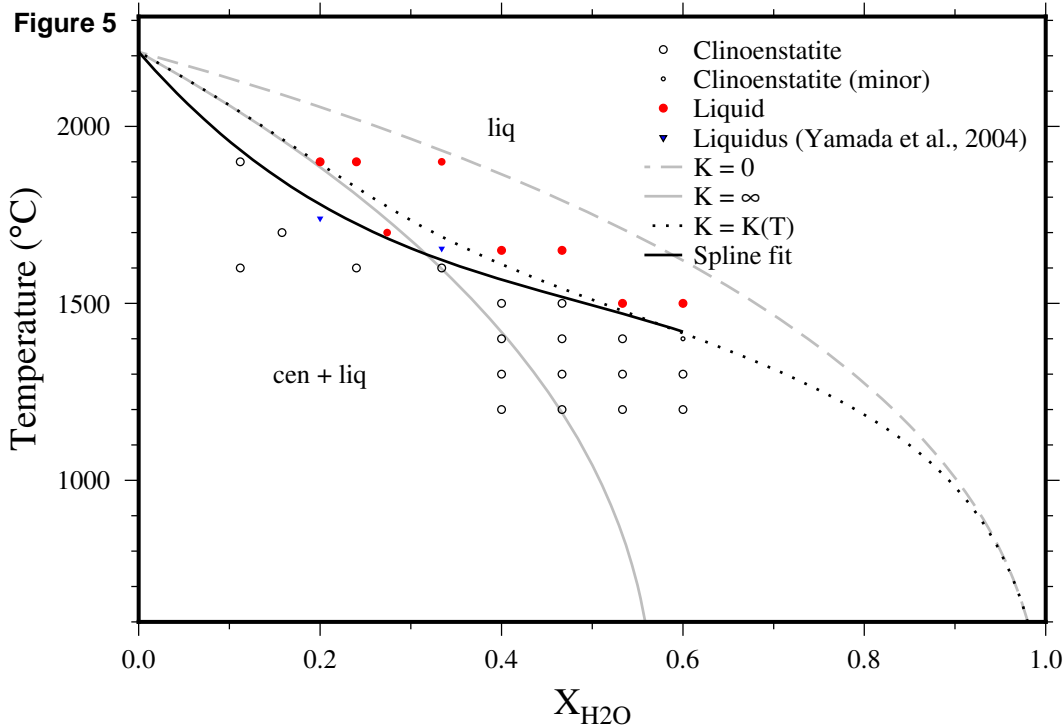
-  *Samples*
-  *Pt₉₀Rh₁₀ capsule and sealing disk*
-  *W-Re Thermocouple*
-  *4-hole alumina*
-  *LaCrO₃ heater*
-  *Molybdenum disk*
-  *Pyrophyllite*
-  *ZrO₂ sheath*
-  *Cr-doped MgO octahedron, sleeves and spacers*

Figure 2









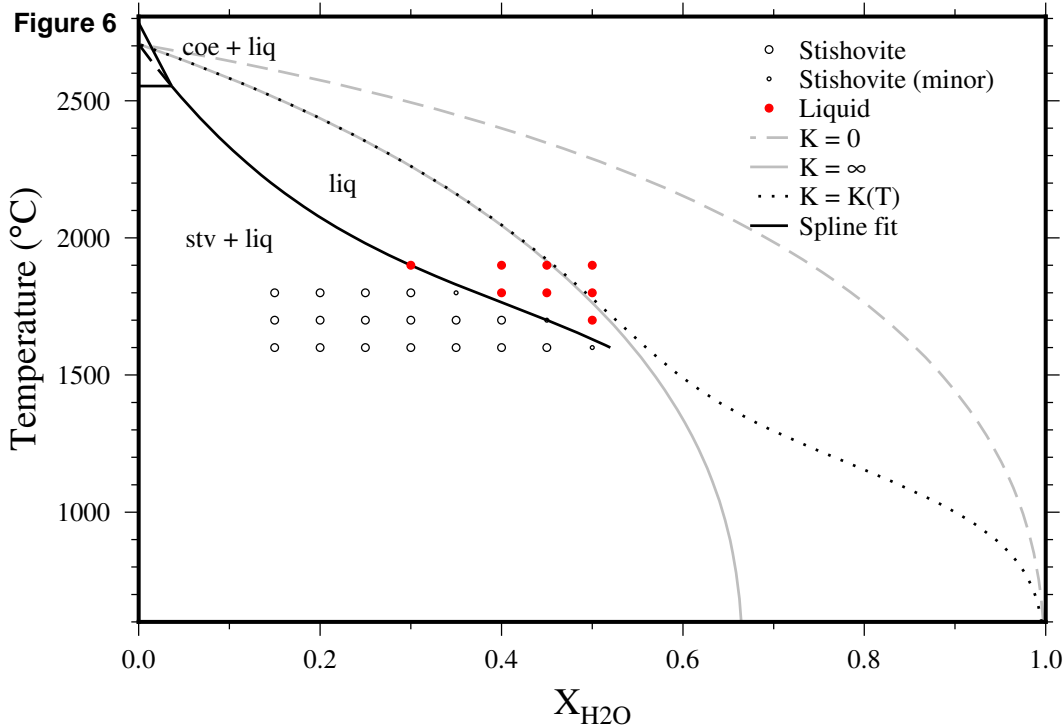


Figure 7

